metals

MDPI

Article

Densification Behavior and Build Quality of Duplex Stainless Steel Fabricated by Laser Powder Bed Fusion

Hongliang Xiang [1,2,*], Guanglei Chen [1], Wei Zhao [1] and Chaochao Wu [1]

[1] School of Mechanical Engineering and Automation, Fuzhou University, Fuzhou 350108, China
[2] Fujian Science & Technology Innovation Laboratory for Optoelectronic Information, Fuzhou 350108, China
* Correspondence: hlxiang@fzu.edu.cn

Abstract: A systematic study on the densification behavior and build quality of 2205 duplex stainless steel fabricated using laser powder bed fusion (LPBF) was performed by experiment and simulation, aiming to offer some supplementary work for research on additive manufacturing (AM) of duplex stainless steel. In this study, samples with differing laser powers were prepared, and a highest relative density of 98.87% was obtained. Then, the pore defects and surface morphologies were investigated to unveil densification behaviors during a building process. The relationship between surface morphologies and the formation of pores was discussed. It reveals that the inter-layer printing on these surface defects caused by unreasonable laser power could increase the possibility of inside pore defects and reduce the density of specimens. Particularly, the big spatters could be the cause of lack-of-fusion defects even under sufficient power input. Therefore, adequate intra- and inter-layer bonding under reasonable processing parameters is crucial for densification. The mechanical properties of the specimens prepared with the laser power of 260 W are the highest, and the yield strength, tensile strength, and elongation are 798.68 MPa, 953.63 MPa, and 10.85%, respectively.

Keywords: laser powder bed fusion; densification behavior; surface quality; build quality; 2205 duplex stainless steel

Citation: Xiang, H.; Chen, G.; Zhao, W.; Wu, C. Densification Behavior and Build Quality of Duplex Stainless Steel Fabricated by Laser Powder Bed Fusion. *Metals* **2023**, *13*, 741. https://doi.org/10.3390/met13040741

Academic Editor: Hany Hassanin

Received: 14 February 2023
Revised: 4 April 2023
Accepted: 10 April 2023
Published: 11 April 2023

1. Introduction

Additive manufacturing (AM) is an advanced manufacturing technology integrating materials, machinery, computers, and other disciplines [1] for application in fields such as the medical and aerospace ones [2,3] and exhibits capabilities of fabricating metals [4], ceramic [5,6], organic polymers [7] and biological materials [8]; more materials and applications have been reviewed by Yap et al. [9] and Zhao et al. [10]. Metal additive manufacturing (MAM) is an important branch of AM, mainly involving directed energy deposition (DED) [11] and powder bed fusion (PBF) [12,13]. DED differs from PBF in the way of forming: DED is to supply raw materials simultaneously during the melting process, however, PBF involves a fusion process after laying the powder bed. Moreover, usually, PBF has higher printing accuracy than DED [14]. Laser powder bed fusion (LPBF) that belongs to PBF can build metallic parts with complex structures without relying on a mold. The part built with suitable process parameters could have excellent precision and be of high quality [15,16], which can broaden the application field of metal materials [17].

In addition to comparing the microstructure and properties of additive manufacturing and traditional manufacturing [18,19], the influence of processing parameters on build quality is also the focus of research [20,21]. The common processing parameters in LPBF include laser power, scanning speed, hatch space, and so on. How to coordinate building parameters is vital to obtaining desired parts with high density and high performance. Nigon et al. [22] printed 2205 steel with a density of 98.6% by matching laser power and scanning speed; the tensile strength and elongation of the specimen were 872 MPa and 11%, respectively. Hu et al. [18] used μ-LPBF to fabricate 316 L steel that has high elongation

(over 40%) without sacrificing the high strength (795 MPa). The degree of influence of different processing parameters on the build quality is not the same. Some researchers designed orthogonal experiments to compare the influence of various processing parameters on the build quality of LPBF. Huang et al. [23] studied the influence of processing parameters on the top surface and vertical surface roughness of the built parts, where the laser power was revealed to have the greatest influence. In conclusion, reasonable matching of manufacturing parameters is crucial to obtain high-quality parts, where laser power plays a significant role. Improper parameters reduce the surface quality and density, resulting in the deterioration of performance. Hence, some researchers optimized the process using Artificial Intelligence (AI) technology. Phadke et al. [24] used Artificial Neural Networks to enhance the dimensional accuracy of the LPBF process, which enables the user to optimize the print parameter without actually printing. However, the densification behavior during printing and the correlation between surface quality and internal build quality is not yet clear, where a comprehensive understanding is required to further improve the process.

Duplex stainless steel is a recent example. Although widely used in industries like marine and petrochemical because of superior mechanical properties and corrosion resistance [25], the application of duplex stainless steel was severely restricted for intricate parts due to the different softening mechanisms and poor coordination of ferrite and austenite under conventional processing technologies [26]. The LPBF technology has opened new avenues for fabricating complex components of duplex stainless steel. Cui et al. [27] mixed austenite stainless steel powder and super duplex stainless steel powder to achieve balanced duplex microstructures. However, existing research on LPBF manufacturing of duplex stainless steel mainly focuses on the effect of post-heat treatment on microstructure and properties [28–30], and a comprehensive description of the influence of process parameters on microstructure and properties of as-built duplex stainless steel is still lacking. Therefore, this paper aims to offer some supplementary work for research on additive manufacturing of duplex stainless steel.

In this paper, the densification behavior and build quality of LPBF-fabricated duplex stainless steel were studied systematically. Various build qualities were obtained by changing the most crucial parameter of laser power. Then, the relative density and pore defects, surface morphology and quality, microstructure and mechanical properties of specimens were analyzed to clarify the densification behaviors and build quality. In particular, the internal relationship between surface quality and the inside build quality during a printing process, and the different mechanisms of lack-of-fusion defect are discussed. In addition, the effect of the big spatter defect on densification behavior was analyzed by simulation. This could provide an important reference for the fabrication of high-quality duplex stainless steel via LPBF.

2. Materials and Methods

2.1. Powder Characterization and Printing Preparation

First, 2205 duplex stainless steel powders were fabricated by the gas atomization method. The chemical composition (wt.%) of 2205 power is determined as Cr (22.13), Ni (5.52), Mo (3.25), Si (0.11), N (0.18), C (0.017), P (0.007), S (0.0045), and a balance of Fe, which conforms to the composition standard of 2205 duplex stainless steel. Figure 1a shows the morphology of powder; the shape of almost all powder particles is near-spherical, and just a small portion of particles have an irregular shape. The sphericity of particles is 93.08%. The powder size distribution measured by the BT-9300S Laser Particle Size Analyzer is illustrated in Figure 1b; the red bars represent the volume fraction of different size powders, and the cumulative volume fraction is shown by the purple curve. The main particle size ranges from 15–53 μm and exhibits a mean particle size D50 of 28.65 μm, which is satisfied for LPBF forming.

In this research, the device used to manufacture specimens is the Metal M2. The LPBF manufacturing parameters were set as depicted in Table 1: scan speed of 800 mm/s, hatch

space of 70 μm, layer thickness of 30 μm, and laser power in the range of 140–320 W. The volumetric energy of printing parameters can be calculated by the following equation:

$$E_V = \frac{P}{V \times H \times T} \quad (1)$$

where P, V, H, T represent laser power, scan speed, hatch space, and layer thickness, respectively. Volumetric energies can directly reflect the laser energy input. The volumetric energy is changed by changing the power in this experiment.

The scanning strategy is intra-layer S-type scanning and the inter-layer rotation is 67°, as shown in Figure 1c. To prevent the oxidation of molten metal, high-purity argon was filled into the forming cavity before printing, and the oxygen content in the building process was kept at less than 300 ppm until printing was done. Specimens with the dimension of 8 mm × 8 mm × 10 mm were manufactured to analyze the pore defects and microstructure. Moreover, dumbbell-shaped tensile samples were built to investigate the mechanical properties. The specific size of the tensile sample is given in Figure 1d. The samples were catted at the bottom by a wire cut electric discharge machine after the LPBF printing; the cutting direction was perpendicular to the building direction.

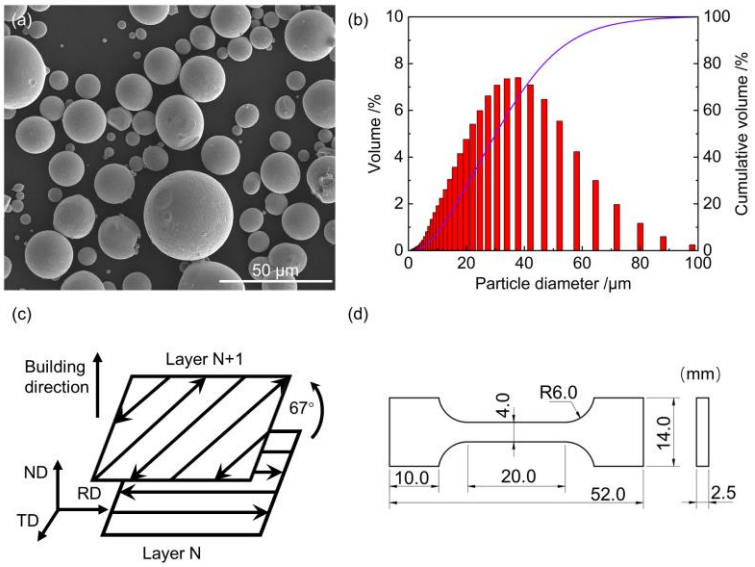

Figure 1. (**a**) Powder morphology captured by SEM; (**b**) size distribution of powder; and the schematic maps of (**c**) scanning strategy and (**d**) tensile sample.

Table 1. The LPBF process parameter for fabricating 2205 duplex stainless steel.

Laser Power (W)	Scan Speed ($mm \cdot s^{-1}$)	Hatch Space (μm)	Layer Thickness (μm)	Volumetric Energies ($J \cdot mm^{-3}$)
140	800	70	30	83.33
200	800	70	30	119.05
260	800	70	30	154.76
320	800	70	30	190.48

2.2. Microstructure Characterization and Property Test

The density of the specimen was measured based on the Archimedes principle. Each specimen was measured three times by Sartorius BSA 224S, then the measurement result was used to calculate the relative density (the theoretical density of 2205 duplex stainless steel is 7.8 $g \cdot cm^{-3}$). The surface of the cross section was pre-ground and polished to a mirror state. After being etched in 9 mL H_2SO_4 + 40 mL H_2O + 0.5 g $KMnO_4$ corrosion solution for 6–8 h, the morphology and pore distribution of the surface were observed

under MV5000 optical microscope (OM). The top surface morphology and tensile fracture morphology of specimens were observed by Nova 230 field emission scanning electron microscopy (SEM). The surface roughness was tested by Surface Roughness Tester TR200. Electron backscattering diffraction (EBSD) was used to obtain phase and grain information (analyzed by OIM), and the observation plane was perpendicular to the building direction. Before EBSD analyses, the surface to be tested was immersed in 8% nitrate-alcohol solution for electrochemical polishing 90 s, and the electrolytic voltage was maintained at about 20 V while polishing. The AG-X plus electronic universal testing machine was used to test the tensile properties of the specimens. Three parallel samples were selected for each group of building parameters, and their arithmetic mean values were calculated. During the tensile test, the loading speed was set at 2 mm·min^{-1}.

2.3. Model Description

To study how surface quality affects the LPBF build quality, a 3-D numerical model was built. The simulation was carried out by ANSYS Fluent 18.0, a computational fluid dynamics (CFD) software. It is known that the LPBF process is accompanied by complex physical phenomena, involving heat absorption of laser beam, heat transfer, melting, evaporation and cooling of metals, Marangoni flow, etc. The transformation of mass, momentum, and energy during the LPBF process follows conservation equations, which are expressed as follows [31–33]:

Mass conservation equation

$$\frac{\partial \rho}{\partial t} + \nabla \cdot (\rho \vec{u}) = 0 \tag{2}$$

Momentum conservation equation

$$\frac{\partial (\rho \vec{u})}{\partial t} + \nabla \cdot (\rho \vec{u} \otimes \vec{u}) = -\nabla p + \nabla \cdot (\mu \nabla u) + S_H \tag{3}$$

Energy conservation equation

$$\frac{\partial (\rho H)}{\partial T} + \nabla \cdot (\rho \vec{u} H) = \nabla \cdot (k \nabla T) + Q_H \tag{4}$$

where ρ, μ, H, and k represent density, dynamic viscosity, specific enthalpy, and thermal conductivity of material; $\vec{u}$ is the flow velocity; p is the pressure; T is the temperature; S_H is the momentum source term induced by surface tension, frictional dissipation in the mushy zone, and recoil force; and Q_H is the energy source term that involves the energy input by laser and the heat loss due to the evaporation of metal.

The heat source used in this calculation following a Gaussian distribution is described by Equation (5):

$$q_{laser} = \frac{2\eta P}{\pi r^2} exp \frac{-2\left[(x - x_0)^2 + (y - y_0)^2\right]}{r^2} \tag{5}$$

where η is the laser absorption coefficient of material; P is laser power; r is laser spot radius; and x_0 and y_0 indicate the laser spot center position, which changes with time. The main thermophysical properties of 2205 duplex stainless steel applied in calculation are given in Table 2, which are referenced from literature [34–36]. The thermal conductivity and specific heat are also provided in Figure 2, both of which are increased by temperature. The particle size ranges from 10 μm to 50 μm, and particles are randomly distributed on a substrate whose properties are set up to resemble the powder. There is no preheat process before printing so the initial temperature of substrate and powder bed is set as 300 K. In this model, mixed energy dissipation in the form of radiation and convection on boundary is considered.

Table 2. Thermophysical properties of 2205 duplex stainless steel applied in simulation.

Property	Value
Solidus temperature (K)	1658
Liquidus temperature (K)	1773
Solidus density ($kg \cdot m^{-3}$)	7860
Liquidus density ($kg \cdot m^{-3}$)	7200
Latent heat of fusion ($J \cdot kg^{-1}$)	5×10^5
Viscosity of liquid ($kg \cdot m^{-1} \cdot s^{-1}$)	0.0085
Surface tension ($kg \cdot s^{-2}$)	1.6
Temperature coefficient of surface tension ($kg \cdot s^{-2} \cdot K^{-1}$)	-9.25×10^{-4}

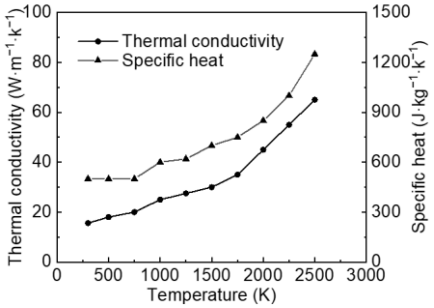

Figure 2. Thermal conductivity and specific heat of 2205 duplex stainless steel used in model.

3. Results and Discussion

3.1. Relative Density

Figure 3 depicts the relationship between laser power and relative density. When laser power is 140 W, the relative density is 97.69%, which gradually increases along with the raise of laser power. The relative density of the specimen fabricated by 260 W is 98.78%, which is the maximum value in the present investigation. However, as laser power increased further, the density began to decrease. Relative density decreased to 97.98% when the laser power was raised to 320 W. In a word, the density of the specimen increased first and then decreased with the increase in laser power. It could be considered that the variation of sample density induced by the laser power increase is mainly related to pores.

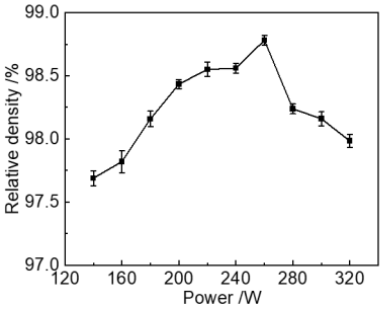

Figure 3. Relationship between laser power and relative density.

To reveal why the density varies with laser power, the samples of 140 W, 200 W, 260 W, and 320 W were picked out from Figure 3 to observe the pore defects; the corresponding relative density was 97.69%, 98.43%, 98.78%, and 97.98%, respectively. Figure 4 gives the pore distribution on the surface of the cross-section. Figure 4a shows that when the laser power is 140 W, the surface has some large size pores and there are unfused powders mixed in the pores. With the increase in laser power, the number and the size of pores decrease gradually. When the laser power is increased to 260 W, the melted tracks arrange neatly and dense metallurgical bonding is formed; only a few small-sized pores exist in local areas, as shown in Figure 4c. However, the large-sized pore appears again when the laser power is raised to

320 W. In conclusion, the number and the size of pores increase first, and then decrease with the increase in laser power, which is consistent with the variation trend of specimen density.

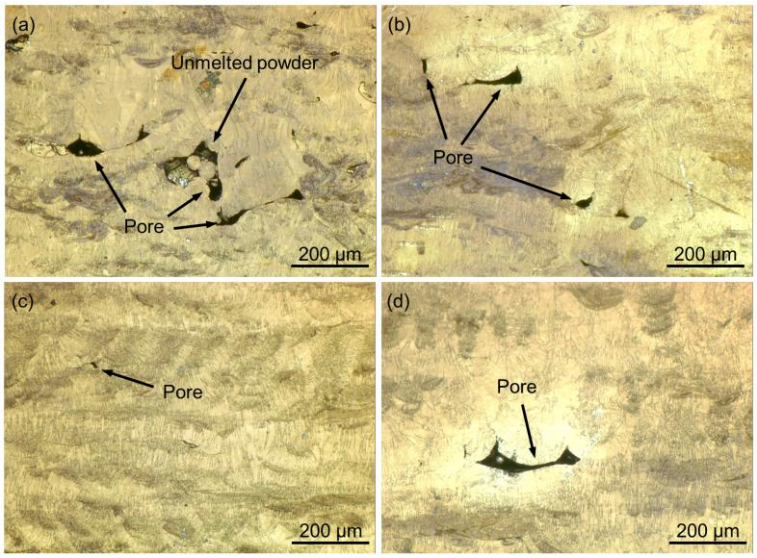

Figure 4. Pores distribution in cross-section: (**a**) 140 W, (**b**) 200 W, (**c**) 260 W, and (**d**) 320 W.

3.2. Surface Morphology

It is generally believed that while the printing process is stable, the surface morphology of each layer exhibits similar characteristics, although the local specific morphologies may differ due to the stochastic nature of powder size and distribution. This enables us to estimate the inside building process via the top surface morphology. Therefore, the top surface morphology of samples was observed to unveil the formation mechanisms of pore defects. Figure 5 is the surface morphology of specimens captured by SEM, and the measurement result of surface roughness is shown in Figure 6. Figure 5a shows that when the laser power was 140 W, there were some balling particles and depressions on the surface. This is due to the energy input being insufficient, meaning that the powder could not be fully melted; the temperature of the molten pool is lower, and the surface tension of the molten pool was too high. Under the action of high surface tension, the spreading of the molten pool became difficult, and agglomeration was facilitated. This would also cause necking or fracture in the local area of the melt tracks, even while large balling particles form. The presence of these defects increases the surface roughness; the surface roughness was 7.535 μm. Figure 5b shows that as laser power is increased, the number of depressions is going to decrease, and the roughness decreases to 7.208 μm. When laser power is raised to 260 W, a smooth surface is obtained, in which the melted tracks are continuous and arrange neatly, and obvious defects are not observed, as shown in Figure 5c. The surface roughness of 260 W was 7.143 μm. At that point, the energy input was reasonable, the powder was fully melted, and the molten pool spread smoothly to form a good bond, which was conducive to the formation of a flat surface. However, at an even higher laser power of 320 W, some larger-sized splash particles adhere to the surface, reducing the surface quality and increasing the surface roughness. This large size spatter is identified as powder agglomeration spatter in paper [37], the size of which is larger than other types of powder. This is owing to the laser power being too high, which leads to the temperature of the molten pool going beyond the evaporating temperature. In this case, although the powder particle could be fully melted, the molten liquid is prone to evaporation. The molten pool would be hit downward by the evaporation recoil pressure and oscillate violently, causing part of the melt to push out by vapor jet from the molten pool and form liquid spatters. These liquid spatters capture feedstock powders along the travel path on the powder bed or collide with other spatters and coalesce into a larger

spatter. Eventually, these spatters are balled under the action of surface tension, adhere to the surface, and deteriorate surface quality.

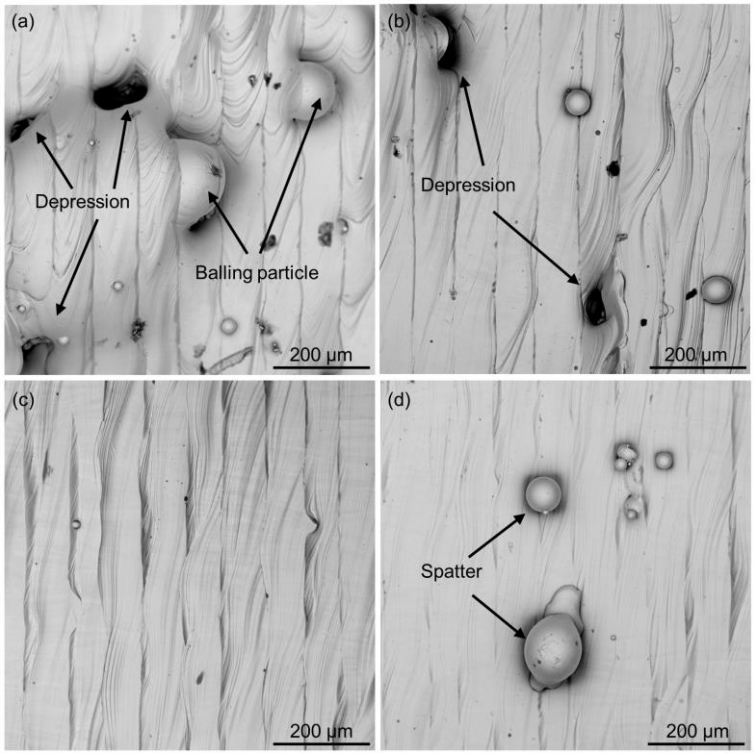

Figure 5. Top surface morphology of samples: (**a**) 140 W, (**b**) 200 W, (**c**) 260 W, and (**d**) 320 W.

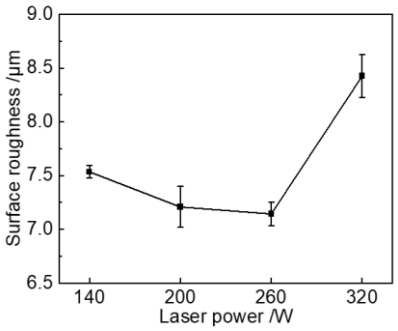

Figure 6. Top surface roughness of samples.

Therefore, proper laser power can effectively suppress the generation of surface defects and improve the surface quality of part, whereas unreasonable laser power leads to defects: depression and balling induced by inadequate laser power, and large size spatter induced by excessive laser power. These surface flaws will deteriorate the surface quality of a part and possibly accelerate the formation of defects during subsequent printing processes.

Combined with the variation of density and pore defects, it can be found that specimens with poor surface quality have more pore defects and lower density. On the other hand, specimens with high surface quality have fewer pore defects and higher density. To reveal the internal relationship between surface quality and pore defects, a schematic diagram of defect generation was drawn based on Figures 4 and 5, as shown in Figure 7. Figure 7a–c illustrate two generation mechanisms of lack-of-fusion defect in specimens with lower power (140 W and 200 W). In Figure 5a,b, depressions and balling defects on the surface as a result of insufficient energy input for low laser power can be clearly observed. When the feedstock powders spread on the prior layer, some of the powder particles slipped into the depressions and the bottom of the balling defects, as shown in

Figure 7a,b, which caused local powder thickness beyond the depth that the laser energy can melt. When these regions were scanned by the laser, the temperature of the powders in the deeper layer could not be raised to the melting point and formed pore defects at these regions. When laser power is appropriate (260 W), the surface of the specimen is flat, and no depression and balling defect exist. At this time, the metallurgical bonding between layers is tight, the defects are fewer, and the density is higher. However, a laser power that is too high lead to spatter and ultimately reduces the surface quality. Figure 7c shows that when the feedstock powders spread on the prior layer, the large spatter particle lifts the scraper upward, increasing the local powder thickness and leading to the formation of a bulge. During laser scanning, due to the limit of the depth of laser energy transport, the powder under the thicker area could not be completely melted, promoting the formation of unfused defects. In summary, suitable laser power can effectively improve surface quality, reducing internal defects and printing high-density specimens.

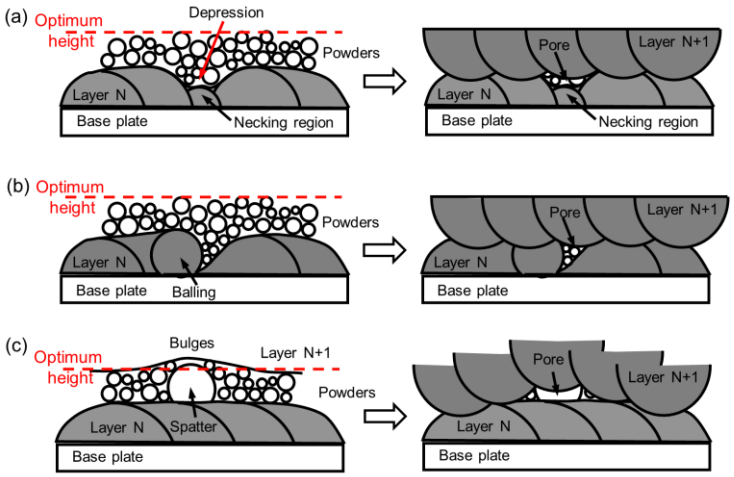

Figure 7. Influence of defects on powder spreading: (**a**) depression; (**b**) large size balling particle; and (**c**) large size spatter.

As shown in Figure 8, a simplified model was built to discuss how the large size spatter promotes the formation of pores. Considering that the size of the spatter particle, which is over 90 μm, is larger than the size of the laser spot, just scanning once is not enough. To avoid this situation, the laser beam scans from the outside of the powder until the spatter is completely scanned, just as Figure 6 shows. Laser power, scanning speed, and hatch space were set as 320 W, 800 mm/s, and 70 μm, respectively. The large spatter particle size was 150 μm, which is close to the size of the biggest spatter in Figure 5d.

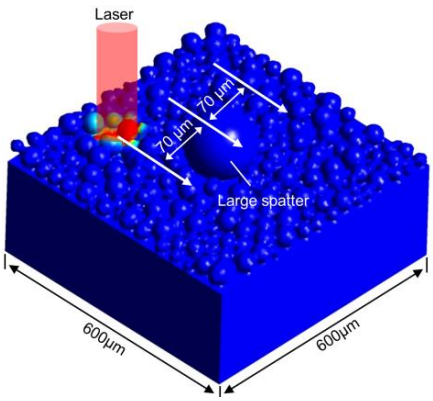

Figure 8. Schematic map of the model.

The result of the simulation is illustrated in Figure 9a. It was found that the spatter was not melted completely, and a cavity existed at the bottom of the spatter. This cavity

is likely to be left in the sample in the form of pores in the subsequent printing process, preventing the acquisition of a dense material. Three cross-sections in different tracks along the scanning direction were cut to observe the melting process of the powder bed and the spatter, and the forming process of pore defects, as shown in Figure 9b. Those sections at different times are shown in Figure 10. In the first melt track, the melt pool did not flow forward with the laser beam and moved on after the laser beam touched the spatter particle. As the laser left the spatter, just a small part of spatter particle scanned by the laser melted, and the regions obscured by the spatter could not be heated and melted via the heat transfer from the melted area. Those regions could also not be filled by the melt pool due to the agglomeration effect of adjacent powders [38] and transformed into a cavity as it cooled down fully, as shown in Figure 10a. In the second melt track, the melt pool stopped flowing forward when the laser touched the spatter particle due to the blocking effect of large particles. Then, the spatter began to melt and flew down to combine with the melt pool. As the laser was fully illuminated on the spatter, quite a part of the spatter was melted and flew outward from the center of the area heated by the laser and combined with the melt pool at this point. However, the region under the particle also could not be melted or filled, as in the first track, and formed a pore defect, as shown in Figure 10b. As seen in Figure 10c, the situation in the third track was different from the previous tracks. Given the heat accumulation caused by the previous tracks, the area scanned by the laser could be melted fully and filled a part of the cavity from the previous tracks. After letting it completely cool, no cavities or pores could be found in the section.

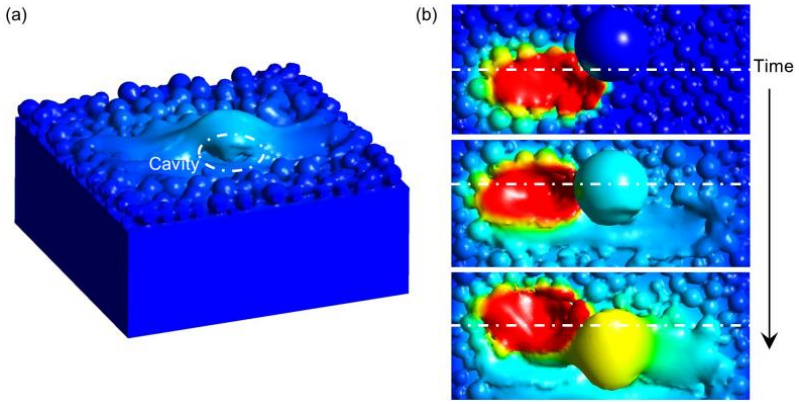

Figure 9. (**a**) Simulation result and (**b**) the positions of three cross-sections in different tracks along the scanning direction. From top to bottom are the first, second, and third track.

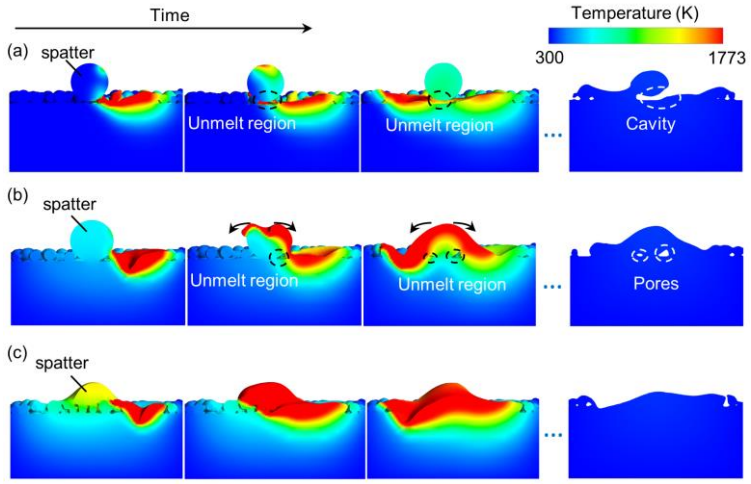

Figure 10. Cross-sections in different tracks indicating the formation induced by large spatter: (**a**) first track, (**b**) second track, and (**c**) third track.

3.3. Microstructure

Figure 11 shows the phase image of samples fabricated with different laser powers, and the Inverse Pole Figure (IPF) in the build direction of the specimen is displayed in Figure 12. In Figure 11, the regions covered by green present ferrite, and the remaining regions covered by red are austenite. Three different regions were randomly selected from the scan surface of each sample to count the phase fraction, and the count results are provided in Figure 13a. It was found that the microstructure of as-built duplex stainless steel fabricated via LPBF is mainly austenite, and only a few ferrites exist. In other papers [30,39–41], LPBF was also used to fabricate duplex stainless steel, and an as-built microstructure with nearly 100% ferrite content was also obtained. This is mainly due to the cooling rate of the metal being as high as 10^4–10^6 K·s^{-1} during the LPBF process, which inhibited the transition from high temperature ferrite to austenite [30,40].

The average grain size of the as-built specimens was calculated according to IPF; the results are shown in Figure 13b. Figure 12a shows that when the laser power was 140 W, the microstructure was mainly composed of fine equiaxed crystals with a few coarsen equiaxed crystals in local areas, and the average grain size was about 1.73 µm. As laser power was raised, the number of fine equiaxed crystals gradually decreased, whereas the number of coarsen equiaxed crystals gradually increased, resulting in grain coarsening on the whole. The average grain size of the specimens prepared with a laser power of 200 W and 260 W was about 1.85 µm and 2.16 µm, respectively, as shown in Figure 12b,c. When the laser power was increased to 320 W, the grains were coarsened further, and the coarsened equiaxed grains existed in the specimen microstructure. The fine equiaxed grains and coarse equiaxed grains were alternately distributed, and the average grain size increased to 3.15 µm. It could be concluded that the grain size increased gradually with the increase in laser power, which is mainly due to the following two reasons. First, with the increase in laser power, the molten pool temperature increases, the cooling velocity decreases, the metal crystallization undercooling degree decreases, and the critical nucleation radius increases, which significantly reduces the nucleation rate. Secondly, the decrease in cooling velocity extends the time spent by molten metal in the high temperature zone, which is conducive to the growth of grain. Therefore, the increase in laser power leads to an increase in grain size, which is consistent with the conclusion of the paper [42].

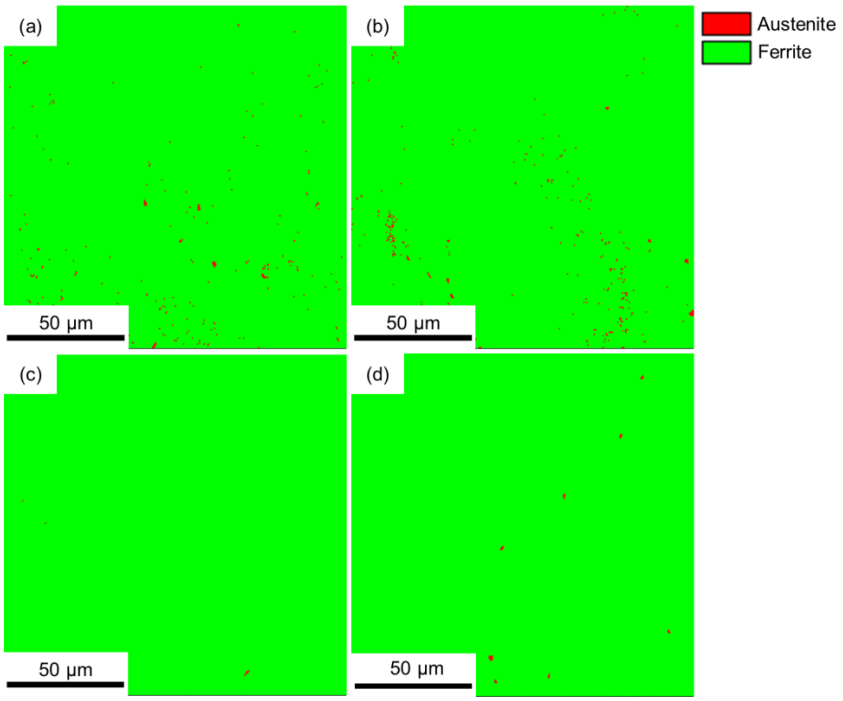

Figure 11. Phase image of specimens: (**a**) 140 W, (**b**) 200 W, (**c**) 260 W, and (**d**) 320 W.

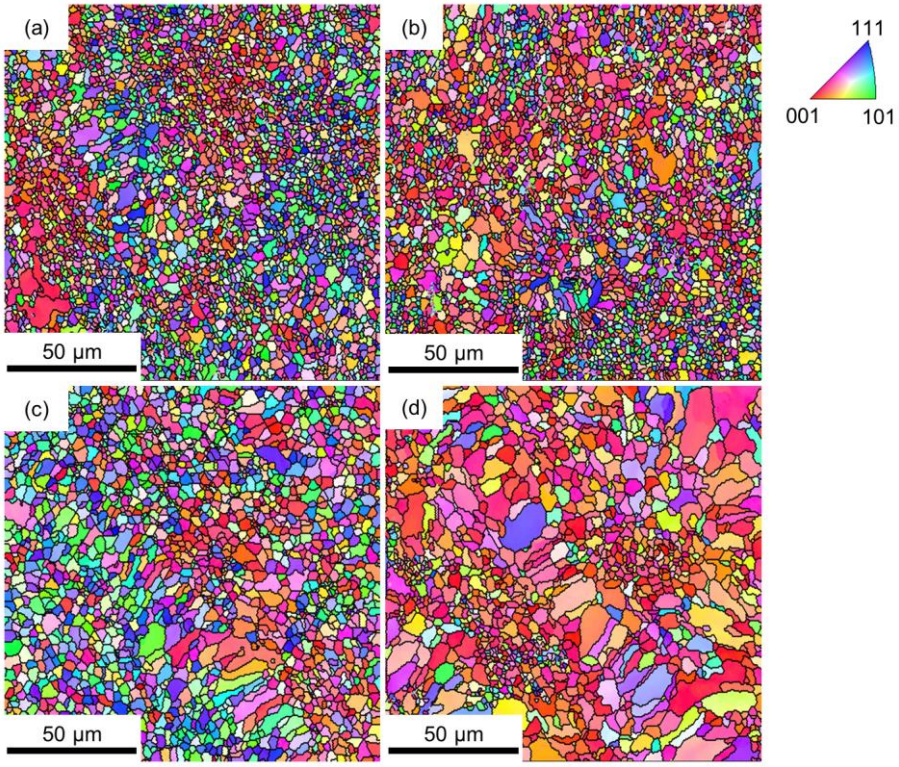

Figure 12. Inverse Pole Figure of specimens: (**a**) 140 W, (**b**) 200 W, (**c**) 260 W, and (**d**) 320 W.

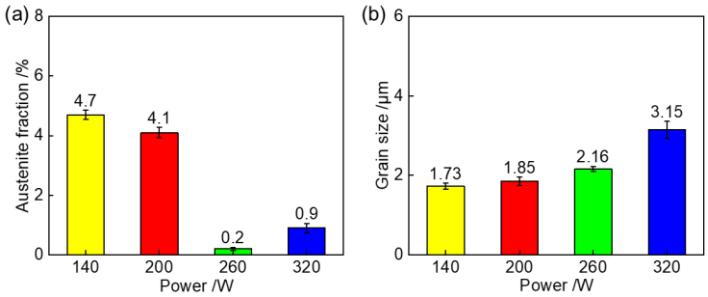

Figure 13. (**a**) Austenite fraction and the (**b**) grain size of the specimens with different power.

3.4. Mechanical Properties

The stress–strain curves and statistics of the mechanical properties of specimens fabricated by different laser powers are given in Figure 14. The yield strength (0.2 YS), tensile strength (UTS), and elongation (EL) of the specimen were 324.73 MPa, 530.24 MPa, and 5.09%, respectively, when the laser power was 140 W, and gradually increased along with the increase in laser power. The yield strength and tensile strength of the specimen fabricated by 260 W reached the peak values of 798.68 MPa and 953.63 MPa, respectively, and the elongation also increased to 10.85%. However, when the laser power was raised further, the yield strength and tensile strength of the specimen began to decrease, whereas the elongation increased slightly to 11.69% when the laser power was 320 W. It could be concluded that the yield strength and tensile strength first increase and then decrease with the increase in laser power, whereas the elongation increased continuously. It is explained in Section 3.3 that the microstructures of the as-built specimens are almost ferrite and the grain size increases with the raise in laser power. According to the Hall-Petch theory [43,44], the strength of the specimens should decrease with an increase in laser power as a result of grain size increases, which is opposed to the tensile test results. This paper considered that the strength varies with the increase in power mainly due to the existence of internal pore defects. When the laser power is too low, there are many unfused pores in the specimen,

resulting in low density and poor mechanical properties. With the increase in laser power, the number of pores decrease and the density increases gradually, and the mechanical properties improve. When the laser power is too high, the number of pores increases and the mechanical properties decrease. It is worth noting that, although the number of pores of the specimen is more than that of the specimen at 260 W when the laser power is 320 W, the elongation of the specimen is slightly increased, which might be related to the significant increase in metallurgical bonding strength. In conclusion, pore defects have a great influence on mechanical properties, and the generation of pore defects can be inhibited by adjusting the laser power to improve the mechanical properties of materials.

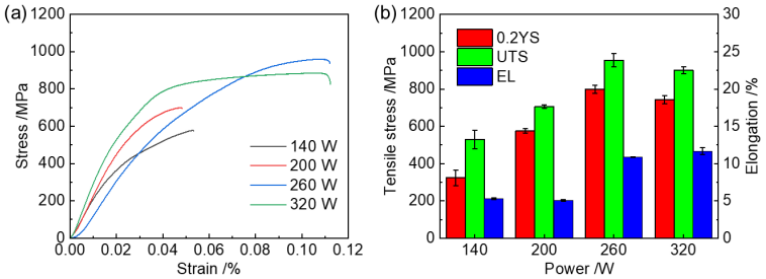

Figure 14. (**a**) Stress–strain curve of specimens and (**b**) statistics of mechanical properties.

In order to explore the fracture mechanism of the specimen, SEM was used to observe the tensile fracture morphology of the specimen; the results are shown in Figure 15. Figure 15a shows that a large area of river pattern and dimples existed in the tensile fracture surface of the specimen formed by 140 W laser, indicating that the fracture mechanism was a ductile-brittle fracture. At the same time, it can be observed that there were holes in the section, which are the potential sources of the crack. Under the action of stress, these holes can easily develop into cracks and spread rapidly, undermining the microstructure and accelerating the fracture of the material, which is the main reason for the low elongation of the specimen. With the increase in laser power, the river pattern area decreased gradually and the number of dimples increased. When the laser power was 260 W, the fracture section was mainly composed of dimples, and no obvious cleavage was found, indicating that the fracture mechanism was a ductile fracture with good plasticity. Figure 15d shows that when the laser power reached 320 W, the fracture morphology of the specimen was a little different from that at 260 W. It was composed of a large number of small dimples that were also ductile fractures.

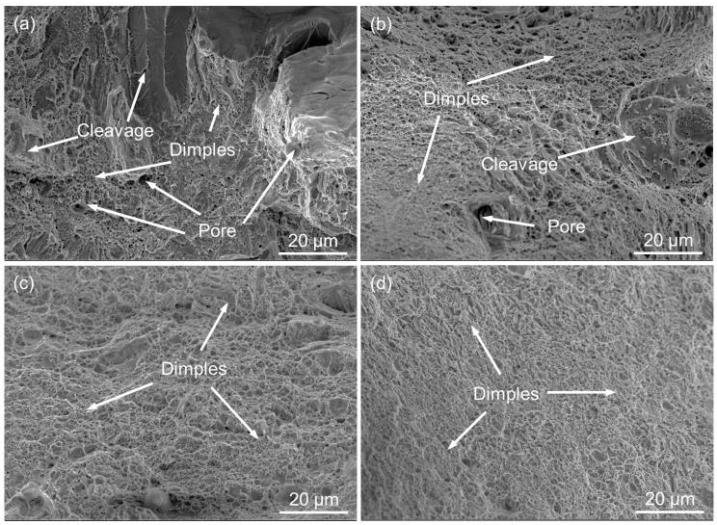

Figure 15. Fracture morphology of specimens: (**a**) 140 W, (**b**) 200 W, (**c**) 260 W, and (**d**) 320 W.

4. Conclusions

This paper studied the densification behavior and build quality of LPBF-fabricated duplex stainless steel, where the relative density and pore defects, surface morphology and quality, microstructure, and mechanical properties were systematically analyzed, and the mechanisms of lack-of-fusion were discussed. The major conclusions drawn are as follows:

1. The laser power has a significant influence on surface quality and density of the LPBF-fabricated part of duplex stainless steel. Proper laser power can promote the formation of a good metallurgical combination, improve surface quality, and inhibit the generation of pore defects. Inappropriate laser power will lead to depression defects balling and splashing particles on the surface of the sample, reducing surface quality, increasing the possibility of lack-of-fusion defects, and reducing the density of the sample. In this paper, when the laser power was 260 W, the surface quality of the sample was optimal, resulting in the highest density of 98.78%.
2. There is an internal relationship between surface quality and internal build quality. Excellent surface quality corresponds to a well-built internal structure by ensuring the quality of the powder layer, which is conducive to suppressing the generation of pore defects and improving the density of the sample. However, on the poor surface morphologies with defects such as large-size depression, balling, and spatters, the local powder layer thickness is increased after powder spreading, resulting in pore defects once it exceeds the laser energy penetration depth.
3. The mechanical properties of the LPBF part are greatly affected by laser power. With the increase in laser power, the tensile strength and yield strength of the sample increase first and then decrease, whereas the elongation of the sample increases continuously. The pore defect is considered to be the key factor affecting the mechanical properties of the sample. In this paper, the sample that was printed at 320 W had the best comprehensive mechanical properties; the yield strength, tensile strength, and elongation of the sample were 798.68 MPa, 953.63 Mpa, and 10.85%, respectively.

Author Contributions: Conceptualization, G.C. and W.Z.; methodology, G.C. and W.Z.; software, C.W.; validation, G.C. and W.Z.; formal analysis, G.C.; data curation, G.C.; writing—original draft preparation, G.C.; writing—review and editing, W.Z. and C.W.; supervision, H.X.; project administration, H.X.; funding acquisition, H.X. All authors have read and agreed to the published version of the manuscript.

Funding: This research was funded by Independent Deployment of Scientific Research Projects of Mindu Innovation Laboratory, grant number 2021ZZ123; Innovation Fund Project of Fujian Digital Equipment and Flexible Manufacturing Innovation Center of China, grant number CXZX-202001.

Data Availability Statement: Not applicable.

Conflicts of Interest: The authors declare no conflict of interest.

References

1. Jin, Y.; Ji, S.; Li, X.; Yu, J. A scientometric review of hotspots and emerging trends in additive manufacturing. *J. Manuf. Technol. Manag.* **2017**, *28*, 18–38. [CrossRef]
2. Madhavadas, V.; Srivastava, D.; Chadha, U.; Raj, S.A.; Sultan, M.T.H.; Shahar, F.S.; Shah, A.U.M. A review on metal additive manufacturing for intricately shaped aerospace components. *CIRP J. Manuf. Sci. Technol.* **2022**, *39*, 18–36. [CrossRef]
3. Ngo, T.D.; Kashani, A.; Imbalzano, G.; Nguyen, K.T.; Hui, D. Additive manufacturing (3D printing): A review of materials, methods, applications and challenges. *Compos. Part B Eng.* **2018**, *143*, 172–196. [CrossRef]
4. Gardner, L. Metal additive manufacturing in structural engineering—Review, advances, opportunities and outlook. *Structures* **2023**, *47*, 2178–2193. [CrossRef]
5. He, R.; Zhou, N.; Zhang, K.; Zhang, X.; Zhang, L.; Wang, W.; Fang, D. Progress and challenges towards additive manufacturing of SiC ceramic. *J. Adv. Ceram.* **2021**, *10*, 637–674. [CrossRef]
6. Sun, J.; Ye, D.; Zou, J.; Chen, X.; Wang, Y.; Yuan, J.; Liang, H.; Qu, H.; Binner, J.; Bai, J. A review on additive manufacturing of ceramic matrix composites. *J. Mater. Sci. Technol.* **2022**, *138*, 1–16. [CrossRef]
7. Weyhrich, C.W.; Long, T.E. Additive manufacturing of high-performance engineering polymers: Present and future. *Polym. Int.* **2022**, *71*, 532–536. [CrossRef]

8. Distefano, F.; Pasta, S.; Epasto, G. Titanium Lattice Structures Produced via Additive Manufacturing for a Bone Scaffold: A Review. *J. Funct. Biomater.* **2023**, *14*, 125. [CrossRef]
9. Yap, C.Y.; Chua, C.K.; Dong, Z.L.; Liu, Z.H.; Zhang, D.Q.; Loh, L.E.; Sing, S.L. Review of selective laser melting: Materials and applications. *Appl. Phys. Rev.* **2015**, *2*, 041101. [CrossRef]
10. Zhao, C.; Lv, Q.; Wu, W. Application and prospects of hydrogel additive manufacturing. *Gels* **2022**, *8*, 297. [CrossRef]
11. Hossein Nedjad, S.; Yildiz, M.; Saboori, A. Solidification behaviour of austenitic stainless steels during welding and directed energy deposition. *Sci. Technol. Weld. Join.* **2022**, *28*, 1–17. [CrossRef]
12. Kuo, Y.-L.; Kamigaichi, A.; Kakehi, K. Characterization of Ni-based superalloy built by selective laser melting and electron beam melting. *Metall. Mater. Trans. A* **2018**, *49*, 3831–3837. [CrossRef]
13. Sing, S.L.; Yeong, W.Y.; Wiria, F.E. Selective laser melting of titanium alloy with 50 wt% tantalum: Microstructure and mechanical properties. *J. Alloys Compd.* **2016**, *660*, 461–470. [CrossRef]
14. DebRoy, T.; Wei, H.; Zuback, J.; Mukherjee, T.; Elmer, J.; Milewski, J.; Beese, A.M.; Wilson-Heid, A.; De, A.; Zhang, W. Additive manufacturing of metallic components—Process, structure and properties. *Prog. Mater. Sci.* **2018**, *92*, 112–224. [CrossRef]
15. Wei, H.; Bhadeshia, H.; David, S.; DebRoy, T. Harnessing the scientific synergy of welding and additive manufacturing. *Sci. Technol. Weld. Join.* **2019**, *24*, 361–366. [CrossRef]
16. Yang, Y.; Chen, J.; Song, C.; Wang, D.; Bai, Y. Current status and progress on technology of selective laser melting of metal parts. *Laser Optoelectron. Prog.* **2018**, *55*, 011401. [CrossRef]
17. Yin, Y.; Tan, Q.; Bermingham, M.; Mo, N.; Zhang, J.; Zhang, M.-X. Laser additive manufacturing of steels. *Int. Mater. Rev.* **2022**, *67*, 487–573. [CrossRef]
18. Hu, Z.; Gao, S.; Zhang, L.; Shen, X.; Seet, H.L.; Nai, S.M.L.; Wei, J. Micro laser powder bed fusion of stainless steel 316L: Cellular structure, grain characteristics, and mechanical properties. *Mater. Sci. Eng. A* **2022**, *848*, 143345. [CrossRef]
19. Srivastava, A.K.; Dubey, A.; Kumar, M.; Dwivedi, S.P.; Sing, R.; Kumar, S. Measurement of form errors and comparative cost analysis for the component developed by metal printing (DMLS) and stir casting. *Instrum. Meas. Metrol.* **2020**, *19*, 363–369. [CrossRef]
20. Maurya, N.K.; Srivastava, A.K.; Saxena, A.; Dwivedi, S.P.; Ashraf Ali, M.; Mustafa, J. Experimental investigation on the effect of laser powder bed fusion process variables on dimensional accuracy, surface roughness and cylindricity of the AlSi10Mg alloy component. *Proc. Inst. Mech. Eng. Part E J. Process Mech. Eng.* **2021**. [CrossRef]
21. Pinto, F.; Aota, L.S.; Souza Filho, I.R.; Raabe, D.; Sandim, H.R.Z. Recrystallization in non-conventional microstructures of 316L stainless steel produced via laser powder-bed fusion: Effect of particle coarsening kinetics. *J. Mater. Sci.* **2022**, *57*, 9576–9598. [CrossRef]
22. Nigon, G.N.; Isgor, O.B.; Pasebani, S. The effect of annealing on the selective laser melting of 2205 duplex stainless steel: Microstructure, grain orientation, and manufacturing challenges. *Opt. Laser Technol.* **2021**, *134*, 106643. [CrossRef]
23. Huang, W.; Zhang, W.; Lian, G.; Chen, X.; Lai, Z. Effect of SLM Forming Process Parameters on Surface Roughness of 316LStainless Steel Parts. *Appl. Laser* **2020**, *40*, 35–41.
24. Phadke, N.; Raj, R.; Srivastava, A.K.; Dwivedi, S.; Dixit, A.R. Modeling and parametric optimization of laser powder bed fusion 3D printing technique using artificial neural network for enhancing dimensional accuracy. *Mater. Today Proc.* **2022**, *56*, 873–878. [CrossRef]
25. George, P.; Wins, K.L.D.; Dhas, D.E.J.; George, P. Machinability, weldability and surface treatment studies of SDSS 2507 material-A review. *Mater. Today Proc.* **2021**, *46*, 7682–7687. [CrossRef]
26. Zou, D.-N.; Wu, K.; Han, Y.; Zhang, W.; Cheng, B.; Qiao, G.-J. Deformation characteristic and prediction of flow stress for as-cast 21Cr economical duplex stainless steel under hot compression. *Mater. Des.* **2013**, *51*, 975–982. [CrossRef]
27. Cui, C.; Becker, L.; Gärtner, E.; Boes, J.; Lentz, J.; Uhlenwinkel, V.; Steinbacher, M.; Weber, S.; Fechte-Heinen, R. Laser Additive Manufacturing of Duplex Stainless Steel via Powder Mixture. *J. Manuf. Mater. Process.* **2022**, *6*, 72. [CrossRef]
28. Papula, S.; Song, M.; Pateras, A.; Chen, X.-B.; Brandt, M.; Easton, M.; Yagodzinskyy, Y.; Virkkunen, I.; Hänninen, H. Selective laser melting of duplex stainless steel 2205: Effect of post-processing heat treatment on microstructure, mechanical properties, and corrosion resistance. *Materials* **2019**, *12*, 2468. [CrossRef]
29. Mahale, R.S.; Rajendrachari, S.; Vasanth, S.; Krishna, H.; Kapanigowda, N.S.; Chikkegowda, S.P.; Patil, A. Technology and challenges in additive manufacturing of duplex stainless steels. *Biointerface Res. Appl. Chem.* **2022**, *12*, 1110–1119. [CrossRef]
30. Hengsbach, F.; Koppa, P.; Duschik, K.; Holzweissig, M.J.; Burns, M.; Nellesen, J.; Tillmann, W.; Tröster, T.; Hoyer, K.-P.; Schaper, M. Duplex stainless steel fabricated by selective laser melting-Microstructural and mechanical properties. *Mater. Des.* **2017**, *133*, 136–142. [CrossRef]
31. Sun, Z.; Chueh, Y.-H.; Li, L. Multiphase mesoscopic simulation of multiple and functionally gradient materials laser powder bed fusion additive manufacturing processes. *Addit. Manuf.* **2020**, *35*, 101448. [CrossRef]
32. Tang, C.; Le, K.Q.; Wong, C.H. Physics of humping formation in laser powder bed fusion. *Int. J. Heat Mass Transf.* **2020**, *149*, 119172. [CrossRef]
33. Wu, C.; Zafar, M.Q.; Zhao, H.; Wang, Y.; Schöler, C.; Heinigk, C.; Nießen, M.; Schulz, W. Multi-physics modeling of side roughness generation mechanisms in powder bed fusion. *Addit. Manuf.* **2021**, *47*, 102274. [CrossRef]
34. Daha, M.; Nassef, G.; Abdallah, I.; AbouSeeda, H. Three-dimensional thermal finite element modeling for keyhole plasma arc welding of 2205 duplex stainless steel plates. *Int. J. Eng. Technol.* **2012**, *2*, 720–728.

35. Ghosh, A.; Misra, D.; Acharyya, S. Numerical Simulation of the Laser Welding of 2205 Duplex Stainless Steel. *Int. J. Laser Sci* **2019**, *1*, 293–313.
36. Palmer, T.; Elmer, J.; Babu, S. Observations of ferrite/austenite transformations in the heat affected zone of 2205 duplex stainless steel spot welds using time resolved X-ray diffraction. *Mater. Sci. Eng. A* **2004**, *374*, 307–321. [CrossRef]
37. Young, Z.A.; Guo, Q.; Parab, N.D.; Zhao, C.; Qu, M.; Escano, L.I.; Fezzaa, K.; Everhart, W.; Sun, T.; Chen, L. Types of spatter and their features and formation mechanisms in laser powder bed fusion additive manufacturing process. *Addit. Manuf.* **2020**, *36*, 101438. [CrossRef]
38. Wu, C.; Zhao, H.; Li, H.; Lin, F. Track irregularity behaviours in electron beam selective melting. *Sci. Technol. Weld. Join.* **2023**, *28*, 27–37. [CrossRef]
39. Davidson, K.P.; Singamneni, S.B. Metallographic evaluation of duplex stainless steel powders processed by selective laser melting. *Rapid Prototyp. J.* **2017**, *23*, 1146–1163. [CrossRef]
40. Feng, S.; Xiaoqiu, C.; Peng, Z.; Zuchun, J.; Fei, M.; Shubin, R.; Xuanhui, Q. Novel ferritic stainless steel with advanced mechanical properties and significant magnetic responses processed by selective laser melting. *Mater. Trans.* **2019**, *60*, 1096–1102. [CrossRef]
41. Saeidi, K.; Kevetkova, L.; Lofaj, F.; Shen, Z. Novel ferritic stainless steel formed by laser melting from duplex stainless steel powder with advanced mechanical properties and high ductility. *Mater. Sci. Eng. A* **2016**, *665*, 59–65. [CrossRef]
42. Zhou, Y.; Li, W.; Zhang, L.; Zhou, S.; Jia, X.; Wang, D.; Yan, M. Selective laser melting of Ti–22Al–25Nb intermetallic: Significant effects of hatch distance on microstructural features and mechanical properties. *J. Mater. Process. Technol.* **2020**, *276*, 116398. [CrossRef]
43. Hall, E. The deformation and ageing of mild steel: III discussion of results. *Proc. Phys. Soc. Sect. B* **1951**, *64*, 747. [CrossRef]
44. Petch, N. The cleavage strength of polycrystals. *J. Iron Steel Inst.* **1953**, *174*, 25–28.